JACS
JOURNAL OF THE AMERICAN CHEMICAL SOCIETY
Article
Cite This: J. Am. Chem. Soc. 2018, 140, 2135−2144
pubs.acs.org/JACS

Probing Interactions of N-Donor Molecules with Open Metal Sites within Paramagnetic Cr-MIL-101: A Solid-State NMR Spectroscopic and Density Functional Theory Study

Thomas Wittmann,[†] Arobendo Mondal,[‡] Carsten B. L. Tschense,[†] Johannes J. Wittmann,[§] Ottokar Klimm,[∥] Renée Siegel,[†] Björn Corzilius,[§] Birgit Weber,[∥] Martin Kaupp,*[,‡] and Juergen Senker*[,†]

[†]Inorganic Chemistry III, University of Bayreuth, Universitätsstraße 30, 95447 Bayreuth, Germany
[‡]Institute of Chemistry, Theoretical Chemistry/Quantum Chemistry, Technical University of Berlin, Sekr. C7, Straße des 17. Juni 135, 10623 Berlin, Germany
[§]Institute of Physical and Theoretical Chemistry and Institute of Biophysical Chemistry, Goethe University Frankfurt, Max-von-Laue-Straße 7-9, 60438 Frankfurt am Main, Germany
[∥]Inorganic Chemistry II, University of Bayreuth, Universitätsstraße 30, 95447 Bayreuth, Germany

Supporting Information

ABSTRACT: Understanding host−guest interactions is one of the key requirements for adjusting properties in metal−organic frameworks (MOFs). In particular, systems with coordinatively unsaturated Lewis acidic metal sites feature highly selective adsorption processes. This is attributed to strong interactions with Lewis basic guest molecules. Here we show that a combination of ^{13}C MAS NMR spectroscopy with state-of-the-art density functional theory (DFT) calculations allows one to unravel the interactions of water, 2-aminopyridine, 3-aminopyridine, and diethylamine with the open metal sites in Cr-MIL-101. The ^{13}C MAS NMR spectra, obtained with ultrafast magic-angle spinning, are well resolved, with resonances distributed over 1000 ppm. They present a clear signature for each guest at the open metal sites. Based on competition experiments this leads to the following binding preference: water < diethylamine ≈ 2-aminopyridine < 3-aminopyridine. Assignments were done by exploiting distance sum relations derived from spin−lattice relaxation data and $^{13}C\{^1H\}$ REDOR spectral editing. The experimental data were used to validate NMR shifts computed for the Cr-MIL-101 derivatives, which contain Cr_3O clusters with magnetically coupled metal centers. While both approaches provide an unequivocal assignment and the arrangement of the guests at the open metal sites, the NMR data offer additional information about the guest and framework dynamics. We expect that our strategy has the potential for probing the binding situation of adsorbate mixtures at the open metal sites of MOFs in general and thus accesses the microscopic interaction mechanisms for this important material class, which is essential for deriving structure−property relationships.

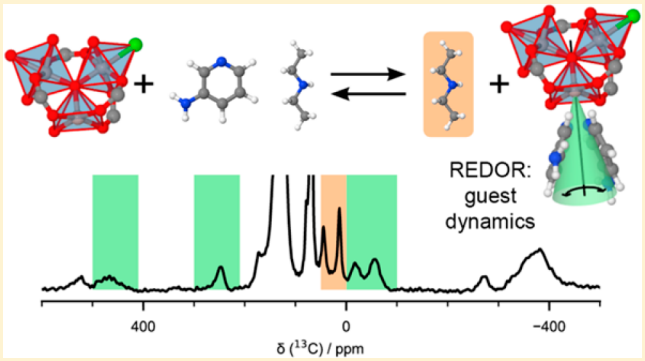

INTRODUCTION

The targeted design of MOFs with chemical functionalities promise advanced applications in the fields of molecular separation[1] and recognition,[2,3] catalysis,[4−6] and drug delivery.[7−9] Such applications crucially rely on selective interactions between the target molecules and the host. Depending on the MOF topology, these interactions are mediated either by the organic linkers[2,10,11] or by strong coordinative interactions between Lewis acidic metal sites and Lewis basic guests.[12−14] Among the latter, aromatic N-heterocyclic compounds like indole,[15−17] carbazole,[15,16] and quinoline[18] derivatives with sizes comparable to the upper limit of micropores (<2 nm) belong to the most environmentally harmful molecules which are, nevertheless, natural components of liquid fuels, petroleum, and refinery streams.[12,13,15,19] Their combustion produces NO_x radicals and contributes to acid rain.[13,19] Considerable effort was made on the removal of such molecules from liquids, in particular with MOFs featuring coordinatively unsaturated metal sites (CUS).[15−20]

Several studies suggest that indeed the formation of coordinative bonds between the CUS and the guest molecules[15,17,18,20] is responsible for the strong adsorption affinities. Adsorption isotherms, calorimetric measurements,

Received: September 22, 2017
Published: January 9, 2018

DOI: 10.1021/jacs.7b10148
J. Am. Chem. Soc. 2018, 140, 2135−2144

and thermogravimetric experiments coupled to an infrared (IR) or a mass spectrometer allow for the determination of adsorption enthalpies and binding preferences.[15,17,19] By combination of microscopic techniques like fluorescence,[21] UV−vis,[22] and Raman/IR[23] spectroscopy as well as solid-state NMR spectroscopy on diamagnetic MOFs,[24,25] considerable progress was made on unraveling active binding sites, and first insights into the microscopic interaction mechanism were provided.

Various MOF types with CUS host paramagnetic transition metal cations like Cu^{2+} in HKUST-1,[26] Ni^{2+} and Co^{2+} in CPO-27,[15,27] and Cr^{3+} and Fe^{3+} in MIL-100[28] and MIL-101.[7,29] Here we show that for adsorption processes involving CUS in such systems, ssNMR studies offer additional insight. While paramagnetic NMR spectroscopic studies on MOFs are still rare, the method is well developed for structure determination of biomolecules in the liquid state.[30−35] Guest molecules coordinated at the CUS will experience large hyperfine shifts leading to differences of several hundreds of ppm compared to non-coordinated and diamagnetic guest molecules.[36] While individual resonances might be severely broadened, large shift dispersions still result in excellent resolution. Even for guest molecules coordinating to the CUS via similar chemical functionalities, we expect pronounced differences, which are only slightly influenced by local static or dynamic disorder. Additionally, it should be possible to distinguish species directly coordinated to the CUS and physisorbed in the periphery of the framework. This helps determining and separating various active binding sites, as well as to derive binding affinities to the CUS, leading to an improved understanding of host−guest interactions, in particular for competitive adsorption processes in the future.

Our analysis benefits from very fast magic angle spinning,[37] which makes proton broadband decoupling unnecessary and enhances the sensitivity due to suppression of spinning sideband intensities. For the assignment of ^{13}C MAS NMR spectra, we present two different but equivalent approaches. The signals might be assigned either experimentally via a combination of spin−lattice relaxation and REDOR (rotational echo double resonance) experiments,[37−39] or by state-of-the-art DFT cluster calculations of the NMR shifts that not only include all contributions to orbital, contact, and pseudo-contact shifts but also account for the magnetic couplings between the paramagnetic metal sites within the Curie−Weiss regime.[40] While the NMR strategy is generally applicable as long as the materials remain paramagnetic, the theory for calculating hyperfine shifts in magnetically frustrated systems is new and still needs to be validated against experimental data. Both strategies avoid isotope labeling,[41] which is usually expensive and not generally possible for all guests. Based on the assignment, the observed intensity modulations by the REDOR sequence provide information about the local reorientational disorder of guest molecules and framework.[42−44]

The expressiveness of this strategy is demonstrated on the model system Cr-MIL-101,[29] which was treated with solutions of diethylamine (DEA), 2-aminopyridine (2-AP), and 3-aminopyridine (3-AP) as well as binary mixtures thereof. The inorganic building unit (IBU) of Cr-MIL-101[29] consists of Cr_3O clusters, where two out of three Cr^{3+} cations exhibit an accessible CUS. The NMR shifts derived from ^{13}C MAS NMR spectra were interpreted in terms of binding sites and adsorption preferences.

THEORETICAL BACKGROUND

The theoretical description of the nuclear shielding tensor is based, with one small modification, on a modern quantum-chemical implementation[45] of Kurland−McGarvey theory,[46] which derives the pNMR shift tensor from EPR spin Hamiltonian parameters (**g**, hyperfine coupling (HFC), and zero-field splitting (ZFS) tensors). The shielding tensor is then given as[45,47−50]

$$\boldsymbol{\sigma}^I = \boldsymbol{\sigma}^I_{\mathrm{orb}} - \frac{\mu_B}{\hbar\gamma_I k}\left\{\frac{1}{T-\Theta}\right\}\mathbf{g}\cdot\langle\mathbf{SS}\rangle\cdot\mathbf{A}^I \tag{1}$$

$$\langle\mathbf{SS}\rangle = \frac{\sum_{nm} Q_{mn}\langle n|\mathbf{S}|m\rangle\langle m|\mathbf{S}|n\rangle}{\sum_n \exp(-E_n/kT)} \tag{2}$$

$$Q_{mn} = \begin{cases} \exp\left(-\dfrac{E_n}{kT}\right), & E_n = E_m \\ -\dfrac{kT}{E_m - E_n}\left[\exp\left(-\dfrac{E_m}{kT}\right) - \exp\left(-\dfrac{E_n}{kT}\right)\right], & E_n \neq E_m \end{cases} \tag{3}$$

where $\boldsymbol{\sigma}_{\mathrm{orb}}$ is the orbital shielding tensor, μ_B the Bohr magneton, k the Boltzmann constant, $\hbar$ the reduced Planck constant, γ_I the nuclear gyromagnetic ratio of nucleus I, T the absolute temperature, Θ the Weiss constant, **g** the electronic g-tensor of the system, and $\mathbf{A}^I$ the HFC tensor of nucleus I. $\langle\mathbf{SS}\rangle$ is a spin dyadic with the components $\langle S_\varepsilon S_\tau\rangle$ evaluated in the manifold of eigenstates $|n\rangle$, with the eigenenergies E_n, of the ZFS Hamiltonian.[45,48] Further details for eq 1, including the role of the Weiss constant in the temperature denominator, are given in the Supporting Information. From the shielding tensor, the isotropic shift is derived by eq 4,

$$\delta_{\mathrm{iso}} = \sigma_{\mathrm{ref}} - \frac{1}{3}\mathrm{Tr}[\boldsymbol{\sigma}^I] \tag{4}$$

where σ_{ref} is the isotropic shielding constant of a diamagnetic reference compound and $\mathrm{Tr} = \sigma_{xx} + \sigma_{yy} + \sigma_{zz}$. δ_{iso} includes the Ramsey-type orbital shift (orb), the Fermi-contact (FC), and the pseudo-contact (PC) contributions to the isotropic shift (eq 5):

$$\delta_{\mathrm{iso}} = \delta_{\mathrm{orb}} + \delta_{\mathrm{FC}} + \delta_{\mathrm{PC}} \tag{5}$$

The hyperfine interaction also leads to a shortening of spin−lattice (T_1) and spin−spin (T_2) relaxation times.[31,36,51] The small T_2 and the anisotropic part of the bulk magnetic susceptibility, which is not completely removed by magic-angle spinning, are the main reasons for signal broadening of paramagnetic compounds.[31,52,53] The observed spin−lattice relaxation rates of nuclei in paramagnetic solids probed at high fields are usually dominated by the paramagnetic dipolar relaxation rate, since the Fermi contact contribution becomes negligible due to its dependence of the electronic Larmor frequency (eq S2). $T_1^{\mathrm{para,dipolar}}$ depends on the distance r and on the electron-correlation time τ_s (eqs S3 and S8). Since τ_s only depends on the transition between the electron Zeeman levels, it is considered to be constant for each metal ion independent from the coordinated ligands. The observed relaxation rate $1/T_1^{\mathrm{para}}$ for a specific nucleus is then given by eq 6,

DOI: 10.1021/jacs.7b10148
J. Am. Chem. Soc. 2018, 140, 2135−2144

$$\frac{1}{T_1^{\text{para}}} = \sum_{i=1}^{N} \frac{1}{T_1^{\text{Cr}^i}} = \sum_{i=1}^{N} \frac{\text{const}}{r_{M^i}^6} = \text{const} \cdot \sum_{i=1}^{N} \frac{1}{r_{M^i}^6} = \text{const} \cdot R \tag{6}$$

where R is the distance sum to all paramagnetic centers M^i in its neighborhood. As a consequence, the ratio of the spin−lattice relaxation rates for the two resonances, ref and x, depends only on the ratio of the distance sums R for the corresponding nuclei (eq 7). This will be used as a cost function to rank structure models derived from quantum-chemical calculations (a more detailed discussion is given in the Supporting Information).

$$R_x = \frac{T_1^{\text{ref}}}{T_1^x} R_{\text{ref}} \tag{7}$$

RESULTS AND DISCUSSION

Characterization of X@Cr-MIL-101. Synthesis and activation of H_2O@Cr-MIL-101 and DEA@Cr-MIL-101 were performed according to modified literature procedures starting from $Cr(NO_3)_3 \cdot 9H_2O$ and benzene-1,4-dicarboxylic acid (bdc).[54] Subsequently, H_2O@Cr-MIL-101 and DEA@Cr-MIL-101 were grafted with 2-aminopyridine (2-AP) and 3-aminopyridine (3-AP) by equilibrating the activated MOFs with 0.25 M 1,4-dioxane solutions. This concentration guarantees sufficiently high loadings to occupy all favored adsorption sites without completely filling the pores.

All samples have been characterized by powder X-ray diffraction, elemental analysis including atomic absorption spectroscopy, IR spectroscopy, nitrogen physisorption, and solution ^{1}H NMR spectroscopy after digestion of the products. In all cases the integrity of the MIL-101 framework[11,55] remains intact. The incorporation of DEA, 2-AP, and 3-AP is demonstrated by the appearance of their characteristic stretching vibration bands.

The derived stoichiometries (Table 1) prove that water can be replaced by DEA, 2-AP, and 3-AP. However, for DEA@Cr-MIL-101 an equivalent of 0.5 water molecules remain in the formula unit while an equivalent of 1.76 DEA molecules is adsorbed. While activated Cr-MIL-101 takes up 3.5 and 4.5 equiv of 2-AP and 3-AP, respectively, the samples blocked with DEA adsorb significantly less 2-AP (1.8 equiv) and 3-AP (3.4 equiv). The amount of incorporated DEA remains constant even after exchanging with 2-AP and 3-AP. Interestingly, the total amount of adsorbed guest molecules (H_2O, DEA, 2-AP, and 3-AP) exceeds the number of available CUS (two out of three Cr^{3+} cations), indicating that for all samples both coordinated and non-coordinated guests are present. The reduction of the apparent BET surface areas, which is roughly halved from H_2O@Cr-MIL-101 (~3000 $m^2\ g^{-1}$) to 3-AP +DEA@Cr-MIL-101 (~1687 $m^2\ g^{-1}$), and the decrease of the pore sizes by ca. 0.5 nm seem to correlate with the amount of adsorbed guest molecules, which increases from DEA over 2-AP, 3-AP, and DEA + 2-AP to DEA + 3-AP (Table 1). Further details of the basic characterization are given in the Supporting Information.

Table 1. Determined Formula Units of the Compounds X@Cr-MIL-101, with X = H_2O, 2-AP, 3-AP, DEA, 2-AP + DEA, and 3-AP + DEA

X	formula unit
H_2O	$Cr_3O(H_2O)_2(OH)_{0.8}(NO_3)_{0.2}(bdc)_3$
DEA	$Cr_3O(H_2O)_{0.5}(DEA)_{1.76}(OH)_{0.8}(NO_3)_{0.2}(bdc)_3$
2-AP	$Cr_3O(2\text{-}AP)_{3.5}(OH)_{0.8}(NO_3)_{0.2}(bdc)_3$
3-AP	$Cr_3O(3\text{-}AP)_{4.5}(OH)_{0.8}(NO_3)_{0.2}(bdc)_3$
2-AP + DEA	$Cr_3O(2\text{-}AP)_{1.8}(DEA)_{1.75}(OH)_{0.8}(NO_3)_{0.2}(bdc)_3$
3-AP + DEA	$Cr_3O(3\text{-}AP)_{3.4}(DEA)_{1.75}(OH)_{0.8}(NO_3)_{0.2}(bdc)_3$

The magnetic susceptibility χ was measured exemplarily for H_2O@Cr-MIL-101 (Figure S7) as a function of temperature and modeled with a Bleany−Bowers equation consisting of only one coupling constant $J = -13\ cm^{-1}$ (eq S7). The excellent match indicates that the three Cr^{3+} ions form an equilateral triangle ($J = J_{12} = J_{23} = J_{13}$). The g-value of 1.985 matches the one derived from EPR data and DFT calculations (Figure S6, Tables S3 and S4), and the fraction α of isolated Cr^{3+} ions is below 5%. $\chi^{-1}(T)$ above 50 K (Figure S7) obeys the Curie−Weiss law with an effective magnetic moment μ_{eff} of 3.566 μ_B per Cr^{3+} and a Weiss temperature θ of −102 K. μ_{eff} is lowered compared to the "spin-only" value for Cr^{3+} ($\mu_{\text{eff}} = 3.87\ \mu_B$), which agrees well with values observed for isolated Cr_3O clusters.[56] These results hint to an antiferromagnetic interaction between the three Cr^{3+} ions at low temperatures, mediated via a superexchange through the μ_3-oxygen atom and to a lower extent by the carboxylate groups, which each bridge two Cr^{3+} ions.[57,58]

^{13}C MAS NMR Spectroscopy of X@Cr-MIL-101. *Single Adsorption of N-Donor Compounds.* The ^{13}C NMR spectra of H_2O@Cr-MIL-101, 2-AP@Cr-MIL-101, 3-AP@Cr-MIL-101, and DEA@Cr-MIL-101 (Figure 1, right column) exhibit resonances in the typical diamagnetic shift region (0−180 ppm). In addition, hyperfine shifts are observed with positive (180−500 ppm) and negative (−380−0 ppm) signs. For each isotropic resonance, a maximum of two weak spinning sidebands is observed at a spinning speed of 40 kHz, indicating that the magnitude of the anisotropy of the hyperfine shift is below 250 ppm for all observed resonances. Similarly, the ^{1}H anisotropic hyperfine shifts were estimated to 200−240 ppm (Table S6). Such moderate anisotropies suggest a significant flexibility of the bdc units and the adsorbed guest molecules, also explaining the quite narrow signals. Combined with the short spin−lattice times, which allow for very fast sampling, and ultrafast magic angle spinning, spectra with an excellent resolution could be obtained in a reasonable period of time.

Nevertheless, since the classic correlations between shift and chemical fragment are established for diamagnetic compounds only, additional information is needed to assign the ^{13}C MAS spectra. Here we present a strategy based on the combined use of distance relations derived from spin−lattice relaxation experiments[38] and spectral editing relying on a heteronuclear ^{13}C−^{1}H dipolar dephasing induced with a REDOR experiment.[37,39] While most of the resonances can already be assigned by matching experimental distance sums R_x derived from the T_1 ratios (eq 7) to the ones (R_{DFT}) calculated for characteristic structural fragments, the ^{13}C{^{1}H} REDOR data provide complementary information by discriminating between resonances according to the numbers of protons attached to the carbon atoms responsible for the targeted signal.

Even more importantly, deviations between the experimentally observed and expected dephasing values for rigid C, CH, CH_2, and CH_3 units are unequivocally caused by dynamic reorientational processes since the strength of the dipolar coupling between a carbon atom and its covalently bonded protons is well-known and relatively independent of the local structural properties. Reductions of the expected CH and CH_2

DOI: 10.1021/jacs.7b10148
J. Am. Chem. Soc. 2018, 140, 2135−2144

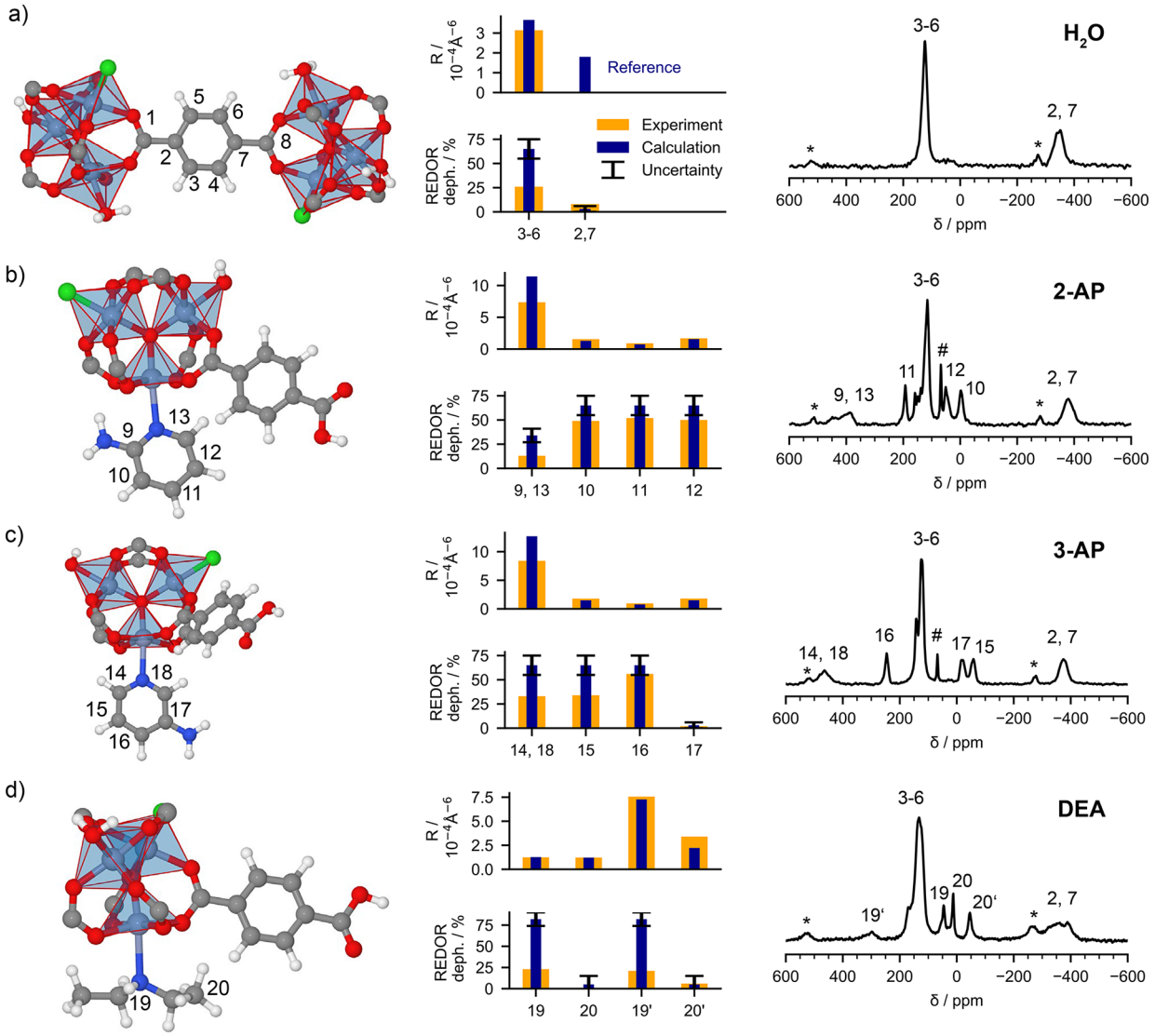

Figure 1. DFT-optimized structural fragments (left column). Comparison between experimental and calculated distance sums and $^{13}C\{^1H\}$ REDOR dephasing values (middle column) and ^{13}C MAS NMR spectra (right column) of (a) H_2O@Cr-MIL-101, (b) 2-AP@Cr-MIL-101, (c) 3-AP@Cr-MIL-101, and (d) DEA@Cr-MIL-101 including assignment. 1,4-Dioxane could be easily removed by evaporation in vacuum, and only traces remain. Key: #, ^{13}C signal of the solvent 1,4-dioxane; *, spinning side bands.

coupling constants have been frequently used to identify motional processes in the past.[42−44] Such analyses provide similar results compared to ^2H NMR studies in the fast motion limit and avoid chemical labeling. We make use of this within our strategy not only to get insight into the preferred adsorption sites and their structural build-up but also to derive a reasonable picture of the local dynamics at the adsorption sites.

For H_2O@Cr-MIL-101, 2-AP@Cr-MIL-101, 3-AP@Cr-MIL-101, and DEA@Cr-MIL-101, we extracted structural fragments (Figures 1 and S8) from the framework, large enough to allow for the calculation of the distance sums R_{DFT} (eq 6) between the Cr^{3+} cations of the IBU and the carbon atoms of both the bdc linkers and the adsorbed molecules, but still small enough to allow for fast structure optimizations at DFT level. The adsorbate molecules were placed at the CUS of the IBU with their Lewis basic centers bonded to the Lewis acidic Cr^{3+} ions and relaxed freely. The calculated distance sum R_{DFT} of one carbon atom was chosen as reference R^{ref}_{DFT}. All the other R_{DFT} values for the other carbon atoms were then compared to the experimental ones (R_x) derived from the ratio of the spin−lattice relaxation times for the reference signal T_1^{ref} and the targeted resonance T_1^x as given in eq 7.

For the reference, we chose the signal at −350 ppm, since it is well separated from any other observed resonance and is present in all four compounds. It exhibits a very small intensity reduction in the $^{13}C\{^1H\}$ REDOR spectra well below 10% (Figures 1 middle column and S9) and thus originates from the quaternary carbon atoms **1**,**8** or **2**,**7** of the bdc linkers. When assigning the atoms **1**,**8** to the reference signal at −350 ppm, R^{ref}_{DFT} calculates to 30.3×10^{-4} Å^{-6} for H_2O@Cr-MIL-101. Using eq 7, R_x for the second observed signal at 130 ppm is calculated based on T_1 (Table S5) to 17.4×10^{-4} Å^{-6}, which is 1 order of magnitude larger compared to the R_{DFT} values for carbon atoms **3**−**6** and **2**,**7** (Figure 1 middle column). In contrast, when assigning carbon atoms **2**,**7** to the reference signal ($R^{ref}_{DFT} = 3.66 \times 10^{-4}$ Å^{-6}), R_x(130 ppm) is 2.10×10^{-4} Å^{-6}, which matches the expectation of $R_{DFT} = 1.80 \times 10^{-4}$ Å^{-6} for the aromatic CH units of the bdc linkers. This assignment is furthermore, supported by the stronger intensity reduction

DOI: 10.1021/jacs.7b10148
J. Am. Chem. Soc. 2018, 140, 2135−2144

within the $^{13}C\{^1H\}$ REDOR spectra, suggesting proton bearing carbon atoms.

The assignment for 2-AP@Cr-MIL-101, 3-AP@Cr-MIL-101, and DEA@Cr-MIL-101 was done in a similar way, and the result is summarized in Figure 1. Additionally, a full list of spin−lattice relaxation times and experimental distance sums is given in Table S5 together with the calculated R_{DFT} values obtained from the model fragments. The general agreement between R_{exp} and R_{DFT} is very good with the exception of the carbon atoms closest to the paramagnetic centers. Examples are the ortho carbon atoms **9,13** of 2-AP as well as **14,18** of 3-AP. With the exception of meta carbon atoms **15,17** for 3-AP@Cr-MIL-101, the T_1 data are decisive enough to assign all resonances. However, for the latter case the intensity modulation of the $^{13}C\{^1H\}$ REDOR spectra allowed to distinguish between the C−NH_2 and C−H units unambiguously.

For DEA two different adsorbate species could be distinguished. While the distance sums for the resonances at 300 and −46 ppm hint to DEA molecules (**19′**, **20′**) coordinated to the CUS, the significantly smaller R values for the signals **19** and **20** at the typical diamagnetic shifts of DEA indicate additional physisorbed DEA species in a second coordination sphere. Taking into account the results of the chemical analysis (Table 1), the CUS are probably occupied by the remaining 0.5 water molecules, and only 1.5 equiv are saturated with DEA molecules. This leaves an equivalent of residual 0.26 DEA molecules uncoordinated but still close to the IBU.

In particular, for 3-AP, DEA, and the bdc linkers, the intensity reduction of the signals for the CH and CH_2 units within the $^{13}C\{^1H\}$ REDOR spectra is considerably less pronounced as expected for rigid CH_x fragments (Figure 1, middle column). The predicted dephasing values were derived using a diamagnetic model system by simulating the intensity reductions for a dephasing time τ_{deph} as short as one rotor period based on the spin-density matrix[59] approach. The effect of the hyperfine interaction during τ_{deph} and the hard 180° pulses on the carbon-13 and proton channels were modeled by treating the anisotropic part of the hyperfine interaction as chemical shift anisotropy. The corresponding coupling constants δ_{hyper} for ^{13}C (Figure 1 right column) and ^1H (Figure S10) were estimated based on spinning sideband intensities of the MAS spectra (a more detailed description is given in the Supporting Information).

For the presented analysis, we used a REDOR sequence with conventional 180° pulses, instead of more advanced recoupling and polarization transfer schemes[60−62] relying on adiabatic pulses. On the one hand, due to the inherent flexibility of the X@Cr-MIL-101 compounds the observed δ_{hyper} are relatively small, allowing for a sufficiently homogeneous excitation with short and hard 180° pulses. On the other hand, adiabatic 180° pulses are inevitably on the same order as τ_{deph} when using ultrafast MAS to match the adiabaticity condition, which makes simulations more demanding and might complicate the extraction of dynamical information from the observed intensity reductions. A detailed description of the model system and the simulations is given in the Supporting Information. Summarizing, without dynamic disorder, we expect intensity reductions of well below 10% for C and CH_3 units and around 65% as well as 80% for CH and CH_2 units, respectively, for the experimentally used conditions of the $^{13}C\{^1H\}$ REDOR experiments (Table S7). Please note that we allow for a variation of roughly 10% for the expected intensity reductions to account for structural changes for the targeted materials and finite size effects within the simulations.

Large deviations between the observed and simulated intensity reductions must be caused by fast large-angle reorientations of guest molecules and bdc linkers, since they are the only motional processes, which influence the dephasing enough on the order of a few tens of μs. To keep the models as simple as possible, we used simple reorientational jump models adapted to the local environment and symmetry to calculate the reduced dipolar coupling constants for the C−H bonds of CH and CH_2 units, following strategies given in refs 37 and 39. The coupling constants were then fed back into the REDOR simulations to derive the dephasing under the influence of motion. We observed that only specific jump models match the observed and calculated dephasing values (Figure 2).

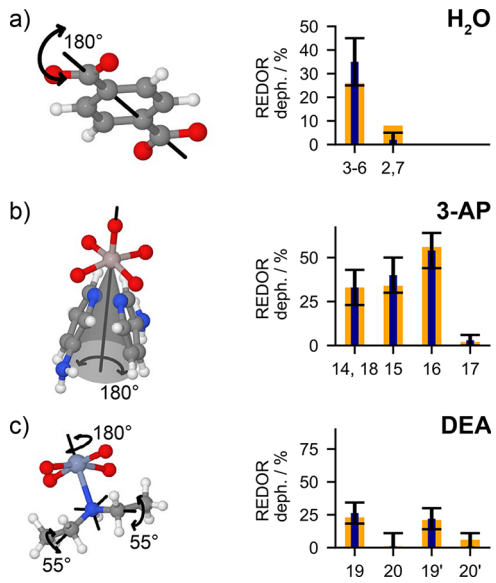

Figure 2. Sketch of the large-angle reorientational jump models (left) used to match the intensity reductions of the $^{13}C\{^1H\}$ REDOR spectra for (a) H_2O@Cr-MIL-101, (b) 3-AP@Cr-MIL-101, and (c) DEA@Cr-MIL-101.

For H_2O@Cr-MIL-101, a fast 180° reorientational jump of the bdc linkers around their C_2 axis reduces the REDOR dephasing of 65% for rigid CH units of the benzene ring to 35% (Figures S16 and S17). We take into account that this process will be accompanied by an additional librational motion reducing the dephasing even further. The match with the experimentally observed dephasing of 26% (Figure 2a) is sound and thus strong evidence that this process is activated and fast at room temperature. Indeed, 180° jumps of the bdc linkers have been observed for various MOFs,[63,64] but were not reported for H_2O@Cr-MIL-101 up to now. For 3-AP only a uniaxial 180° jump of the pyridine ring about the N−Cr bond axis overlaid with a small librational toggling motion on a cone with a half opening angle of 20° (Figure 2b) accounts for the different effect on the CH units in ortho/meta positions (**14**, **15**, **18**) with respect to the one in para position (**16**). In contrast, the steric demand of the ortho amino group in the case of 2-AP hinders both 90° and 180° jumps around the N−Cr axis. Deviations between simulated and observed REDOR dephasings are much less pronounced (Figure 1b middle column) compared to the other guest molecules and are well

DOI: 10.1021/jacs.7b10148
J. Am. Chem. Soc. 2018, 140, 2135−2144

accounted for by small-angle librations. For DEA two large-angle reorientations are necessary to match the simulated and observed intensity reductions within the $^{13}C\{^1H\}$ REDOR spectra. The first is a 180° jump around the N−Cr axis combined with a reorientation of the CH_2 units around the C−N bond with an amplitude of about 55° (Figure 2c), reflecting the high flexibility of the aliphatic amine compared to the aromatic counterparts 2-AP and 3-AP.

For systems with isolated paramagnetic centers, quantum-chemical shift calculations provide an alternative route to a spectral assignment, and they provide further microscopic insight.[65−69] The applicability of eq 1, that includes the Weiss constant to account for residual magnetic couplings in the Curie−Weiss temperature regime for spin-coupled clusters (see refs 40 and 72 for related applications to solid-state calculations), still needs careful validation, which is possible with due to the available experimental NMR data. We thus applied the full formalism of eq 1 at DFT level (cf. Experimental Section and Supporting Information) to the structural fragments displayed in Figure 1 and compared the results with the experimental assignment. While we have computed all terms in eq 1, in the following the main discussion will focus only on the FC contributions. The reason is that our computations confirm the expectation of small g- and ZFS-anisotropies (see g-tensor and ZFS data in Tables S3 and S4, which are in perfect agreement with the measured EPR spectrum, Figure S6). As a consequence, the PC contributions to the isotropic ^{13}C shifts (Table 2 and S8) are small. The observed and calculated ^1H shifts are shown in Figure S18 and Table S9. The orbital shifts reflect the chemical environment of the nucleus in question in a similar way as for diamagnetic analogues (Tables S8 and S9) and will also not be discussed in detail.

The total computed ^{13}C shifts given in Table 2 and S8 do thus reflect particularly the FC contribution and therefore the delocalization of spin density over the ligand framework, as well as to some extent spin polarization effects. The sign and magnitude of the computed ^{13}C (Table 2 and S8) and ^1H (Table S9) hyperfine shifts agree well with experimental data, and the computed data have been helpful in the signal assignment. Notably, the reduction of hyperfine shifts due to the Curie−Weiss regime by a factor $T/(T - \Theta) = 0.761$ for H_2O@Cr-MIL-101 brings computed and experimental shifts into significantly better agreement. We used the experimentally determined reduction factor for all X@Cr-MIL-101 derivatives, since we do not expect large differences for their magnetic susceptibilities compared to the one of H_2O@Cr-MIL-101. This assumption is based on the magnetic properties for molecular compounds with isolated Cr_3O clusters with H_2O and pyridine-based ligands.[57,58,71] The corresponding exchange constants are similar to the one observed for H_2O@Cr-MIL-101 and vary only between 10 and 13 cm^{-1}. Additionally, for a simulation temperature of 325 K, a change of Θ by 20 K only affects the hyperfine shifts by less than 5%. We note that the negative deviations of the g-tensor from the free-electron value only reduce the computed shifts additionally by about 1%.

The shifts may be rationalized to a great extent by the spin-density plots for the cluster models (Figure 3). For H_2O@Cr-MIL-101, ^{13}C nuclei **1**−**8** split into two sets: carbons **2** and **7** have negative spin densities, while the others exhibit positive spin densities. 2-AP@Cr-MIL-101 and 3-AP@Cr-MIL-101 exhibit additionally alternating positive and negative spin densities within the aminopyridine ring. For carbon atoms **9**−**18** we may distinguish negative spin densities for atoms **10**,

Table 2. Comparison of Observed and Calculated Isotropic and Hyperfine ^{13}C Shifts, δ_{iso} (δ_{FC}), for X@Cr-MIL-101[a]

	^{13}C δ_{iso} (δ_{FC})/ppm	
signal	obsd	calcd
	X = H_2O	
1,8	–	1683 (+1503)
2,7	−350 (−523)	−411 (−552)
3,4,5,6	130 (−5)	129 (−6)
	X = 2-AP	
9	415 (+251)	396 (+231)
10	−4 (−116)	−34 (−145)
11	192 (+46)	235 (+89)
12	49 (−65)	−12 (−126)
13	415 (+251)	444 (+288)
	X = 3-AP	
14	468 (+324)	457 (+314)
15	−59 (−187)	−127 (−255)
16	246 (+121)	290 (+165)
17	−20 (−167)	−80 (−227)
18	468 (+324)	459 (+317)
	X = DEA	
19	47	52
20	13	18
19′	300 (+248)	246 (+194)
20′	−46 (−59)	0 (−18)

[a]Detailed analyses in terms of δ_{orb}, δ_{FC}, and δ_{PC} are given in Table S8.

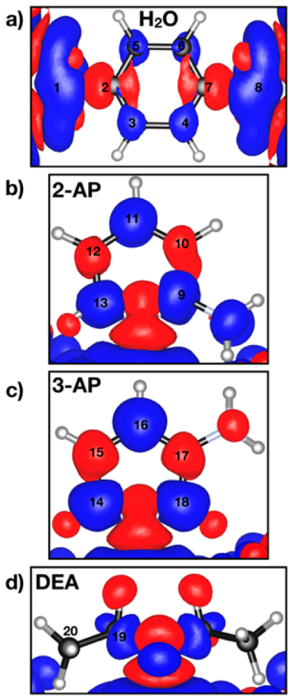

Figure 3. Spin-density plots of (a) H_2O@Cr-MIL-101, (b) 2-AP@Cr-MIL-101, (c) 3-AP@Cr-MIL-101, and (d) DEA@Cr-MIL-101. The blue and red colors represent positive and negative spin-density isosurfaces (±0.0001 au), respectively.

DOI: 10.1021/jacs.7b10148
J. Am. Chem. Soc. 2018, 140, 2135−2144

12, **15**, and **17**, and positive spin densities for the remaining atoms. For DEA@Cr-MIL-101, carbons **19′** and **20′** for the DEA molecules attached to the CUS have positive and negative spin densities, respectively, while the non-coordinated ones (carbons **19** and **20**) exhibit the diamagnetic shifts only.

In all cases, the sign of the assigned hyperfine shifts (see Table 2) agrees perfectly with these spin-density analyses. We note that the extremely large positive spin densities at the carboxyl carbon atoms **1** and **8** in H_2O@Cr-MIL-101 (Figure 3a) give rise to very large positive computed shifts at around +1683 ppm. However, the large positive π-spin density also causes very short transverse (T_2) relaxation times that result in severe signal broadening. As a consequence, the signal disappears in the noise level. In all cases, negative spin densities, and thus negative hyperfine shifts, are due to $\pi-\sigma$-spin polarization mechanisms. Positive spin-delocalization and negative spin-polarization contributions may also partly compensate. Carbon atoms of the linkers **3**–**6** in H_2O@Cr-MIL-101 are examples of such a cancellation (Figure 3a), giving rise to signals near the positions expected for such nuclei in diamagnetic samples (Table 2).[10]

Competitive Adsorption of N-Donor compounds. Based on the results obtained for X@Cr-MIL-101 with X being either H_2O, 2-AP, 3-AP, or DEA, it is now possible to analyze competition experiments with two components. If 3-AP is coadsorbed with 2-AP and DEA, respectively, only the characteristic hyperfine-shifted ^{13}C NMR signals (Figure 4) for 3-AP are observed (**14**–**18**) while for the other components only the typical diamagnetic shifts were found. In contrast, for adsorbate mixtures of 2-AP and DEA both guest molecules show hyperfine-shifted and diamagnetic signals. The most pronounced hyperfine-shifted ones are **11** and **10** of 2-AP and **19′** as well as **20′** of DEA, representative for ligands coordinated to the CUS. Notably, the peaks for coordinated 2-AP are more intense compared to bonded DEA. Consequently, we conclude that the binding strength at the CUS increases in the order H_2O < DEA ≈ 2-AP < 3-AP. This is somewhat surprising as it opposes the chemical intuition that the strongest base 2-AP should exhibit the highest binding affinity. Since the computed binding energies of 142.6 kJ/mol (2-AP) and 143.4 kJ/mol (3-AP) are very similar, we attribute this to the steric hindrance of the amino group in ortho position. The markedly higher mobility of 3-AP (Figure 2) leads to higher entropic contributions to the equilibrium and thus to a stronger binding affinity.

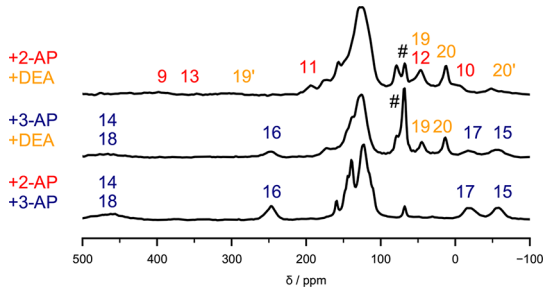

Figure 4. Cutout of the ^{13}C MAS NMR spectra of X@Cr-MIL-101 loaded with two components X = 2-AP + 3-AP (red and blue), 2-AP + DEA (red and orange), and 3-AP + DEA (blue and orange), together with the signal assignment. Key: # ^{13}C signal of the solvent.

Nevertheless, a similar trend was observed for the larger adsorption band for the d-d transitions of Cr^{3+} around 600 nm in the UV–vis spectra of the X@Cr-MIL-101 derivatives (Figure S19). DEA, 2-AP, and 3-AP give rise to increasing blue-shifts with respect to H_2O@Cr-MIL-101, indicating the strongest interaction between Cr^{3+} and 3-AP, while DEA and 2-AP exhibit similar and smaller shifts, respectively. In contrast to the NMR data, which allowed us to distinguish between guest molecules coordinated at the CUS and those physisorbed in a second coordination sphere, the UV–vis spectra are not sufficiently discriminating to answer this question (Figure S19).

The trend of the binding strength seems to be reflected in the magnitude of the hyperfine shifts, if atoms with the same number of bonds away from the paramagnetic center are compared. For example, the hyperfine shifts (δ_{FC}) of the signals for **19′** (DEA), **9**, and **13** (2-AP) as well as for **14** and **18** (3-AP) increase from 248 to 324 ppm (Table 2). However, the same values scatter markedly within the quantum-chemical calculations (Table 2), which indicates that the hyperfine interaction depends not only on the binding strength but also on the structure and the dynamics of the complex and thus on computational aspects such as model construction and method used for structure optimization.

CONCLUSION

H_2O@Cr-MIL-101 was successfully synthesized and loaded with 2-AP, 3-AP, and DEA as well as binary mixtures of these ligands. The well-resolved ^{13}C MAS NMR spectra of the individual Cr-MIL-101 derivatives feature both hyperfine-shifted signals and resonances within the typical shift region of the diamagnetic guest molecules. By combining distance relations derived from spin–lattice relaxation data and structural fragments with REDOR recoupling experiments to group the carbon atoms into C or CH_3 and CH or CH_2 moieties, we were able to unambiguously assign all these resonances. While the hyperfine shifted signals are characteristic for guest molecules coordinated to the CUS, the other resonances represent unspecifically physisorbed guests in a second coordination sphere. In particular, the hyperfine shifted signals present a clear signature for each guest, and thus allow us to decide which of the guest molecules is coordinated to the CUS even for competition experiments using binary mixtures. The derived binding preference depicts the following order: H_2O < DEA ≈ 2-AP < 3-AP.

The experimental assignment has been used to evaluate a computational approach, which amends a modern implementation of the Kurland–McGarvey theory for chemical shifts of systems with arbitrary spin multiplicity by a scaling to the Curie–Weiss regime of magnetically coupled metal centers above the transition temperature. The computed hyperfine shifts are dominated by the Fermi-contact term, which in turn accurately reflects the computed spin-density distributions within the clusters. The Curie–Weiss scaling brings the computed shifts to within about ±20% of the experimental values, also allowing shifts to be predicted in cases where paramagnetic line broadening did not allow detection. This demonstrates the potential of the modified cluster approach to obtain accurate chemical shifts also for exchange-coupled systems like the present MOFs.

Our results show that both the experimental and computational approaches present equivalent assignment strategies and might be used independently in the future. Nevertheless, the NMR experiments offer additional information about the dynamical disorder of the guest molecules and the framework, as the intensity modulations for the $^{13}C\{^1H\}$ REDOR spectra

DOI: 10.1021/jacs.7b10148
J. Am. Chem. Soc. 2018, 140, 2135–2144

of proton-bearing carbon atoms are sensitive to reorientations of the CH bonds. While the bdc linkers as well as the 3-AP and DEA molecules perform fast thermally activated large angle jumps combined with toggling motions, 2-AP molecules coordinated to the CUS are largely immobile. We attribute this to the considerable steric hindrance of the amino function in ortho-position with the IBU.

Our study shows that for the Cr-MIL-101 derivatives, solid-state ^{13}C NMR spectroscopy is well suited to identify the coordinating species as well as to determine their relative interaction strengths, as long as an unambiguous assignment can be achieved. Cr-MIL-101 is, however, only one example among the prominent class of MOFs featuring coordinatively unsaturated sites with paramagnetic metal ions including HKUST, CPO-27, and MIL-100, which were discussed for probing or recovering small gas molecules like CO,[72] CO_2,[73] and H_2[74] as well as for catalysis. All these applications crucially rely on the interaction between the gas molecules and the preferred adsorption sites. The presented strategy has the potential to provide a better understanding for the nature of such host−guest interactions, since it allows one to unveil guest-specific coordination at the CUS, separate them from physisorbed guests, and provide a microscopic picture of the adsorption mechanisms.

EXPERIMENTAL SECTION

Powder X-ray diffraction (PXRD) experiments were carried out in Bragg−Brentano geometry on a Panalytical X'pert Pro diffractometer equipped with a X'Celerator Scientific RTMS detector using Ni filtered Cu Kα radiation (λ = 1.54187 Å, 40 kV, 40 mA). Measurements were made in the range of 2°−30° (2θ) with a step size of 0.017°. The theoretical PXRD pattern was simulated from an optimized structure (using the Universal force field of the Forcite tool implemented in Materials Studio 5.0) obtained from a crystallographic information file.[75] The pattern was simulated with Cu Kα radiation, reflection geometry, and the Pearson profile functions. The half-width of the Bragg reflections was set to 0.15°. The parameters of the cubic cell of the space group $Fd\bar{3}m$ (No. 227) were set to 87.5 nm.

Attenuated total reflectance (ATR) IR spectra were recorded in the range 400−4000 cm^{-1} with a resolution of 4 cm^{-1} on a Jasco FT/IR-6100 spectrometer with a PIKEGladi ATR accessory.

The samples for chemical analyses were prepared in a glovebox under argon atmosphere after evacuating at 90 °C for 2 h. Carbon, hydrogen, and nitrogen contents (wt%) were obtained on a Vario elementar EL III. Chromium contents (wt%) were determined by atomic absorption spectroscopy in extinction mode on a Varian AA100 using a N_2O/acetylene flame upon chemical digestion. EDX spectroscopy was carried out on a Jeol JSM 6400 scanning electron microscope equipped with a Noran energy-dispersive X-ray analyzer and using a beam voltage of 20 kV.

Nitrogen sorption measurements were performed on a Quantachrome Nova 2000e at 77 K after evacuating the adsorbents at 363 K for 2 h under reduced pressure. Brunauer−Emmet−Teller (BET) equivalent surface areas were determined in the relative pressure range between 0.06 and 0.15 to accommodate for microporous materials.[76] Specific total pore volumes were determined at a relative pressure of 0.98 according to the Gurvich rule.[77] The pore-size distributions were derived using the nitrogen NLDFT model at 77 K for the adsorption branch assuming a silica/zeolite surface and a spherical/cylindrical pore shape which is implemented in the Quantachrome ASiQ v3.0 software package.

Dissolving the frameworks in a NaOD/D_2O solution of pH = 8.5 and precipitating the paramagnetic $Cr(OD)_3$ allowed us to record well-resolved solution ^1H NMR spectra and to quantify the modification degrees of both the linkers and IBUs by comparing the signal areas of products with that of the educts.

Diffuse reflectance UV/vis absorption spectra were recorded on an Agilent Cary 300 Scan spectrometer in the range from 190 to 800 nm with scan speeds of 0.5 nm/s.

The magnetic susceptibility data of H_2O@Cr-MIL-101 were collected using a MPMSXL-5 SQUID magnetometer under an applied field of 1591540 A/m over the temperature range 50−400 K. The solid sample was prepared in a gelatin capsule. The agreement factor R between the experimental and simulated data was calculated as $R = \sum_i(\chi_M^{exp} - \chi_M^{sim})^2/\sum_i(\chi_M^{sim})^2$.

The EPR spectrum was recorded at X-band frequencies (9.4 GHz) by sweeping the external magnetic field from 0.1 to 0.6 T. A modulation frequency 100 kHz and an amplitude of 0.2 mT were used. The conversion time was set to 40.96 ms.

^{13}C MAS spectra were acquired using a 1.9 mm triple resonance probe (Bruker) and a spinning speed of 40 kHz. A Hahn-echo pulse sequence with an interpulse distance of 25 μs (one rotor period) was applied for background suppression. Due to fast spinning heteronuclear proton broadband decoupling did not have an influence on the spectral resolution and was thus omitted. The 90° pulse length and recycle delay were set to 2.0 μs and 50ms, respectively. The averaged temperature in the rotor at ν_{rot} = 40 kHz was determined to 325 K by referencing with $Pb(NO_3)_2$.[78] The spin−lattice relaxation times T_1 were obtained with the inversion recovery method with a recycle delay of 0.3 s and time increments ranging from 0.5 to 256 ms. The $^{13}C-^1H$ REDOR-type recoupling experiments were performed with two 180° pulses on the ^1H channel at the center of each of the two rotation periods (τ_{deph} = 50 μs) while a 180° pulse was applied on the ^{13}C at the center of the two rotation periods. ^1H and ^{13}C 180° pulse lengths are 2.8 and 4 μs, respectively.

DFT computations of the ^{13}C and ^1H shifts were done at structures of the four model clusters optimized at PBE0-D3/def2-TZVP level,[79−83] using the Turbomole program.[84] Subsequently, the magnetic-resonance parameters have been computed using appropriate 9s7p4d metal[85] and IGLO-II main-group element[86] basis sets. In these calculations, a ferromagnetically coupled spin arrangement within the cluster has been chosen. The HFC and g-tensor calculations with the ORCA code[87] used a modified PBE40 hybrid functional (PBE0 with increased 40% exact-exchange admixture) that we recently found to perform well for solid-state pNMR shift calculations,[70] and which is also known to give excellent HFCs and g-tensors in relativistic computations for molecules.[88] The computed HFCs have been normalized to the number of spin centers present.[89] ZFS tensors were computed using the PBE exchange-correlation functional[90] and the Pederson−Khanna second-order perturbation approach[91] with van Wüllen's prefactors.[92] For both g-tensors and ZFS, the necessary spin−orbit matrix elements were computed within the spin−orbit mean-field approximation[93] implemented in ORCA. Orbital shieldings were obtained with the PBE40 functional using Gaussian09 (for both open- and closed-shell cases).[94] All pNMR computations have been performed for T = 325 K. The value of the Weiss constant (Θ = −102 K) has been taken from experiment (Figure S7). Both ^1H and ^{13}C shifts were referenced to tetramethylsilane (TMS) at the same level (using a PBE/def2-TZVP structure for TMS; the values are σ_{ref}^C = 189.23 ppm and σ_{ref}^H = 31.68 ppm).

ASSOCIATED CONTENT

Supporting Information

The Supporting Information is available free of charge on the ACS Publications website at DOI: 10.1021/jacs.7b10148.

Detailed description of the theory used for the chemical shift calculations and the spin−lattice relaxation analysis; PXRD pattern, IR spectra, chemical compositions, ^1H liquid NMR spectra, nitrogen sorption isotherms, and pore size distributions of X@Cr-MIL-101 with X = H_2O, DEA, 2-AP, and 3-AP; EPR spectrum and analysis of H_2O@Cr-MIL-101; calculated g- and ZFS-tensors of X@Cr-MIL-101; fit of the magnetic susceptibility χ and χ^{-1} of H_2O@Cr-MIL-101; full DFT-optimized fragment

DOI: 10.1021/jacs.7b10148
J. Am. Chem. Soc. 2018, 140, 2135−2144

clusters of X@Cr-MIL-101; ^{13}C spin−lattice relaxation data and distance sums; $^{13}C\{^1H\}$ REDOR spectra of X@Cr-MIL-101; ^1H MAS NMR spectra of X@Cr-MIL-101; dephasing values of L-histidine·HCl·H_2O with and without the influence of the hyperfine interaction; influence of large angle jumps on the $^{13}C\{^1H\}$ dephasing values of MIL-101; detailed comparison between calculated and observed ^{13}C and ^1H chemical shifts of X@Cr-MIL-101; and UV−vis spectra of X@Cr-MIL-101 (PDF)

SIMPSON inputs for the simulations of the $^{13}C\{^1H\}$ REDOR dephasing for carbons C1 to C6 of histidine as well as for all carbon atoms within 3-aminopyridine and diethylamine adsorbed to the CUS (ZIP)

AUTHOR INFORMATION

Corresponding Authors

*martin.kaupp@tu-berlin.de

*juergen.senker@uni-bayreuth.de

ORCID

Björn Corzilius: 0000-0003-3937-9137

Birgit Weber: 0000-0002-9861-9447

Martin Kaupp: 0000-0003-1582-2819

Notes

The authors declare no competing financial interest.

ACKNOWLEDGMENTS

We gratefully acknowledge financial support by the DFG (SE 1417/7-1 and SFB 840). Work in Berlin has been funded by the EU 7th Framework Programme within the Marie Curie Actions Initial Training Network scheme, under grant agreement no. 317127, the "pNMR project". B.C. has received funding from the Deutsche Forschungsgemeinschaft (DFG) through Emmy Noether grant CO802/2-1; further support from the BMRZ is acknowledged. We thank Beate Bojer for her steady support with the NMR measurements.

REFERENCES

(1) Qiu, S.; Xue, M.; Zhu, G. *Chem. Soc. Rev.* **2014**, *43*, 6116.

(2) Li, Q.; Zhang, W.; Miljanic, O. S.; Sue, C.; Zhao, Y.-L.; Liu, L.; Knobler, C. B.; Stoddart, J. F.; Yaghi, O. M. *Science* **2009**, *325*, 855.

(3) Cai, H.; Li, M.; Lin, X. R.; Chen, W.; Chen, G. H.; Huang, X. C.; Li, D. *Angew. Chem., Int. Ed.* **2015**, *54*, 10454.

(4) Lee, J.; Farha, O. K.; Roberts, J.; Scheidt, K. A.; Nguyen, S. T.; Hupp, J. T. *Chem. Soc. Rev.* **2009**, *38*, 1450.

(5) Czaja, A. U.; Trukhan, N.; Müller, U. *Chem. Soc. Rev.* **2009**, *38*, 1284.

(6) Ma, L.; Abney, C.; Lin, W. *Chem. Soc. Rev.* **2009**, *38*, 1248.

(7) Horcajada, P.; Chalati, T.; Serre, C.; Gillet, B.; Sebrie, C.; Baati, T.; Eubank, J. F.; Heurtaux, D.; Clayette, P.; Kreuz, C.; Chang, J.-S.; Hwang, Y. K.; Marsaud, V.; Bories, P.-N.; Cynober, L.; Gil, S.; Ferey, G.; Couvreur, P.; Gref, R. *Nat. Mater.* **2010**, *9*, 172.

(8) Horcajada, P.; Gref, R.; Baati, T.; Allan, P. K.; Maurin, G.; Couvreur, P.; et al. *Chem. Rev.* **2012**, *112*, 1232.

(9) McKinlay, A. C.; Morris, R. E.; Horcajada, P.; Férey, G.; Gref, R.; Couvreur, P.; Serre, C. *Angew. Chem., Int. Ed.* **2010**, *49*, 6260.

(10) Wack, J.; Ahnfeldt, T.; Stock, N.; Senker, J.; et al. *J. Phys. Chem. C* **2013**, *117*, 19991.

(11) Wittmann, T.; Siegel, R.; Reimer, N.; Milius, W.; Stock, N.; Senker, J. *Chem. - Eur. J.* **2015**, *21*, 314.

(12) Van de Voorde, B.; Bueken, B.; Denayer, J.; De Vos, D. *Chem. Soc. Rev.* **2014**, *43*, 5766.

(13) Samokhvalov, A. *Chem. - Eur. J.* **2015**, *21*, 16726.

(14) Li, J.-R.; Kuppler, R. J.; Zhou, H.-C. *Chem. Soc. Rev.* **2009**, *38*, 1477.

(15) Maes, M.; Trekels, M.; Boulhout, M.; Schouteden, S.; Vermoortele, F.; Alaerts, L.; Heurtaux, D.; Seo, Y.; Hwang, Y. K.; Chang, J.; Beurroies, I.; Denoyel, R.; Temst, K.; Vantomme, A.; Horcajada, P.; Serre, C.; De Vos, D. E. *Angew. Chem.* **2011**, *123*, 4296.

(16) Van de Voorde, B.; Boulhout, M.; Vermoortele, F.; Horcajada, P.; Cunha, D.; Lee, J. S.; Chang, J.; Gibson, E.; Daturi, M.; Lavalley, J.; Vimont, A.; Beurroies, I.; De Vos, D. E. *J. Am. Chem. Soc.* **2013**, *135*, 9849.

(17) Nuzhdin, A. L.; Kovalenko, K. A.; Dybtsev, N.; Bukhtiyarova, G. A. *Mendeleev Commun.* **2010**, *20*, 57.

(18) Ahmed, I.; Khan, N. A.; Hasan, Z.; Jhung, S. H. *J. Hazard. Mater.* **2013**, *250−251*, 37.

(19) Seo, P. W.; Ahmed, I.; Jhung, S. H. *Phys. Chem. Chem. Phys.* **2016**, *18*, 14787.

(20) Ahmed, I.; Jhung, S. H. *Chem. Eng. J.* **2014**, *251*, 35.

(21) Dai, J.; Mckee, M. L.; Samokhvalov, A. *J. Porous Mater.* **2014**, *21*, 709.

(22) Alaerts, L.; Maes, M.; Van Der Veen, M. A.; Jacobs, P. A.; De Vos, D. E. *Phys. Chem. Chem. Phys.* **2009**, *11*, 2903.

(23) Van de Voorde, B.; Boulhout, M.; Vermoortele, F.; Horcajada, P.; Cunha, D.; Lee, J. S.; Chang, J.; Gibson, E.; Daturi, M.; Lavalley, J.; Vimont, A.; Beurroies, I.; De Vos, D. E. *J. Am. Chem. Soc.* **2013**, *135*, 9849.

(24) Devautour-vinot, S.; Martineau, C.; Diaby, S.; Ben-Yahia, M.; Miller, S.; Serre, C.; Horcajada, P.; Cunha, D.; Taulelle, F.; Maurin, G. *J. Phys. Chem. C* **2013**, *117*, 11694.

(25) Čendak, T.; Žunkovič, E.; Godec, T. U.; Mazaj, M.; Logar, N. Z.; Mali, G. *J. Phys. Chem. C* **2014**, *118*, 6140.

(26) Chui, S. S.-Y.; Lo, S. M.-F.; Charmant, J. P. H.; Orpen, A. G.; Williams, I. D. *Science* **1999**, *283*, 1148.

(27) Achmann, S.; Hagen, G.; Hämmerle, M.; Malkowsky, I.; Kiener, C.; Moos, R. *Chem. Eng. Technol.* **2010**, *33*, 275.

(28) Jeremias, F.; Khutia, A.; Henninger, S. K.; Janiak, C. *J. Mater. Chem.* **2012**, *22*, 10148.

(29) Férey, G.; Mellot-Draznieks, C.; Serre, C.; Millange, F.; Dutour, J.; Surblé, S.; Margiolaki, I. *Science* **2005**, *309*, 2040.

(30) Bertini, I.; Luchinat, C.; Parigi, G. *Eur. J. Inorg. Chem.* **2000**, *2000*, 2473.

(31) Bertini, I.; Turano, P.; Vila, A. J. *Chem. Rev.* **1993**, *93*, 2833.

(32) Wicholas, M.; Mustacich, R.; Jayne, D. *J. Am. Chem. Soc.* **1972**, *94*, 4518.

(33) Wilkens, S. J.; Xia, B.; Volkman, B. F.; Weinhold, F.; Markley, J. L.; Westler, W. M. *J. Phys. Chem. B* **1998**, *102*, 8300.

(34) Walker, F. A. *Inorg. Chem.* **2003**, *42*, 4526.

(35) Banci, L.; Bertini, I.; Luchinat, C.; Pierattelli, R.; Shokhirev, N. V.; Walker, F. A. *J. Am. Chem. Soc.* **1998**, *120*, 8472.

(36) Bertini, I.; Luchinat, C.; Parigi, G. *Prog. Nucl. Magn. Reson. Spectrosc.* **2002**, *40*, 249.

(37) Ishii, Y.; Wickramasinghe, N. P.; Chimon, S. *J. Am. Chem. Soc.* **2003**, *125*, 3438.

(38) Wickramasinghe, N. P.; Shaibat, M. A.; Ishii, Y. *J. Phys. Chem. B* **2007**, *111*, 9693.

(39) Wickramasinghe, N. P.; Shaibat, M. A.; Jones, C. R.; Casabianca, L. B.; De Dios, A. C.; Harwood, J. S.; Ishii, Y. *J. Chem. Phys.* **2008**, *128*, 052210.

(40) Kim, J.; Middlemiss, D. S.; Chernova, N. A.; Zhu, B. Y. X.; Masquelier, C.; Grey, C. P. *J. Am. Chem. Soc.* **2010**, *132*, 16825.

(41) Dawson, D. M.; Jamieson, L. E.; Mohideen, M. I. H.; McKinlay, A. C.; Smellie, I. A.; Cadou, R.; Keddie, N. S.; Morris, R. E.; Ashbrook, S. E. *Phys. Chem. Chem. Phys.* **2013**, *15*, 919.

(42) Saalwächter, K. *Prog. Nucl. Magn. Reson. Spectrosc.* **2007**, *51*, 1.

(43) Bärwinkel, K.; Herling, M. M.; Rieß, M.; Sato, H.; Li, L.; Avadhut, Y. S.; Kemnitzer, T. W.; Kalo, H.; Senker, J.; Matsuda, R.; Kitagawa, S.; Breu, J. *J. Am. Chem. Soc.* **2017**, *139*, 904.

(44) Schanda, P.; Meier, B. H.; Ernst, M. *J. Am. Chem. Soc.* **2010**, *132*, 15957.

DOI: 10.1021/jacs.7b10148
J. Am. Chem. Soc. 2018, 140, 2135−2144

(45) Vaara, J.; Rouf, S. A.; Mares, J. *J. Chem. Theory Comput.* **2015**, *11*, 4840.
(46) Kurland, R. J.; McGarvey, B. R. *J. Magn. Reson.* **1970**, *2*, 286.
(47) Pennanen, T. O.; Vaara, J. *Phys. Rev. Lett.* **2008**, *100*, 133002.
(48) Rouf, S. A.; Mares, J.; Vaara, J. *J. Chem. Theory Comput.* **2015**, *11*, 1683.
(49) Cahill, L. S.; Chapman, R. P.; Kirby, C. W.; Goward, G. R. *Appl. Magn. Reson.* **2007**, *32*, 565.
(50) Soncini, A.; Van Den Heuvel, W. *J. Chem. Phys.* **2013**, *138*, 021103.
(51) Bertini, I.; Luchinat, C.; Parigi, G.; Ravera, E. *NMR of Paramagnetic Molecules. Applications to Metalloproteins and Models*, 2nd ed.; Elsevier: Amsterdam, 2016.
(52) Nayeem, A.; Yesinowski, J. P. *J. Chem. Phys.* **1988**, *89*, 4600.
(53) Bertmer, M. *Solid State Nucl. Magn. Reson.* **2017**, *81*, 1.
(54) Hwang, Y. K.; Hong, D.; Chang, J.; Jhung, S. H.; Seo, Y.; Kim, J.; Vimont, A.; Daturi, M.; Serre, C.; Férey, G. *Angew. Chem., Int. Ed.* **2008**, *47*, 4144.
(55) Livage, C.; Guillou, N.; Chaigneau, J.; Rabu, P.; Drillon, M.; Férey, G. *Angew. Chem., Int. Ed.* **2005**, *44*, 6488.
(56) Welo, L. A. *Philos. Mag.* **1928**, *6*, 481.
(57) Honda, M.; Morita, M.; Date, M. *J. Phys. Soc. Jpn.* **1992**, *61*, 3773.
(58) Tadros, A. M.; Royko, M. M.; Kelley, S. P.; Belmore, K.; Rogers, R. D.; Vincent, J. B. *Polyhedron* **2015**, *100*, 17.
(59) Bak, M.; Rasmussen, J. T.; Nielsen, N. C. *J. Magn. Reson.* **2000**, *147*, 296.
(60) Kervern, G.; Pintacuda, G.; Emsley, L. *Chem. Phys. Lett.* **2007**, *435*, 157.
(61) Pell, A. J.; Sanders, K. J.; Wegner, S.; Pintacuda, G.; Grey, C. P. *J. Chem. Phys.* **2017**, *146*, 194202.
(62) Pell, A. J.; Pintacuda, G. *Prog. Nucl. Magn. Reson. Spectrosc.* **2015**, *84*−*85*, 33.
(63) Kolokolov, D. I.; Stepanov, A. G.; Jobic, H. *J. Phys. Chem. C* **2014**, *118*, 15978.
(64) Kolokolov, D. I.; Stepanov, A. G.; Guillerm, V.; Serre, C.; Frick, B.; Jobic, H. *J. Phys. Chem. C* **2012**, *116*, 12131.
(65) Dawson, D. M.; Ke, Z.; Mack, F. M.; Doyle, R. A.; Bignami, G. P. M.; Smellie, I. A.; Buhl, M.; Ashbrook, S. E. *Chem. Commun.* **2017**, *53*, 10512.
(66) Bühl, M.; Ashbrook, S. E.; Dawson, D. M.; Doyle, R. A.; Hrobárik, P.; Kaupp, M.; Smellie, I. A. *Chem. - Eur. J.* **2016**, *22*, 15328.
(67) Benda, L.; Mareš, J.; Ravera, E.; Parigi, G.; Luchinat, C.; Kaupp, M.; Vaara, J. *Angew. Chem., Int. Ed.* **2016**, *55*, 14713.
(68) Novotný, J.; Sojka, M.; Komorovsky, S.; Nečas, M.; Marek, R. *J. Am. Chem. Soc.* **2016**, *138*, 8432.
(69) Rouf, S. A.; Jakobsen, V. B.; Mareš, J.; Jensen, N. D.; Mckenzie, C. J.; Vaara, J.; Nielsen, U. G. *Solid State Nucl. Magn. Reson.* **2017**, *87*, 29.
(70) Mondal, A.; Gaultois, M. W.; Pell, A. J.; Iannuzzi, M.; Grey, C. P.; Hutter, J.; Kaupp, M. *J. Chem. Theory Comput.* **2018**, *14*, 377−394.
(71) Gavrilenko, K. S.; Addison, A.; Thompson, L.; Pavlishchuk, V. V. *Theor. Exp. Chem.* **2004**, *40*, 214.
(72) Chavan, S.; Vitillo, J. G.; Groppo, E.; Bonino, F.; Lamberti, C.; Dietzel, P. D. C.; Bordiga, S. *J. Phys. Chem. C* **2009**, *113*, 3292.
(73) Dietzel, P. D. C.; Besikiotis, V.; Blom, R. *J. Mater. Chem.* **2009**, *19*, 7362.
(74) Kapelewski, M. T.; Geier, S. J.; Hudson, M. R.; Stück, D.; Mason, J. A.; Nelson, J. N.; Xiao, D. J.; Hulvey, Z.; Gilmour, E.; Fitzgerald, S. A.; Head-Gordon, M.; Brown, C. M.; Long, J. R. *J. Am. Chem. Soc.* **2014**, *136*, 12119.
(75) Lebedev, O. I.; Millange, F.; Serre, C.; Van Tendeloo, G.; Férey, G. *Chem. Mater.* **2005**, *17*, 6525.
(76) Thommes, M. *Chem. Ing. Tech.* **2010**, *82*, 1059.
(77) Gurvich, L. *J. Russ. Phys. Chem. Soc.* **1915**, *47*, 805.
(78) Guan, X.; Stark, R. E. *Solid State Nucl. Magn. Reson.* **2010**, *38*, 74.
(79) Weigend, F.; Ahlrichs, R. *Phys. Chem. Chem. Phys.* **2005**, *7*, 3297.
(80) Weigend, F. *Phys. Chem. Chem. Phys.* **2006**, *8*, 1057.
(81) Adamo, C.; Barone, V. *J. Chem. Phys.* **1999**, *110*, 6158.
(82) Grimme, S.; Antony, J.; Ehrlich, S.; Krieg, H. *J. Chem. Phys.* **2010**, *132*, 154104.
(83) Perdew, J. P.; Burke, K.; Ernzerhof, M. *Phys. Rev. Lett.* **1996**, *77*, 3865.
(84) *TURBOMOLE*, V7.0, a development of University of Karlsruhe and Forschungszentrum Karlsruhe; TURBOMOLE GmbH, 2015.
(85) Munzarová, M.; Kaupp, M. *J. Phys. Chem. A* **1999**, *103*, 9966.
(86) Kutzelnigg, W.; Fleischer, U.; Schindler, M. In *NMR Basic Principles and Progress*; Diehl, E., Fluck, E., Günther, H., Kosfeld, R., Seelig, J., Eds.; Springer: Berlin, 1991.
(87) Neese, F. *ORCA*, An Ab Initio, Density Functional and Semiempirical Program Package, V.3, 2012.
(88) Gohr, S.; Hrobárik, P.; Repiský, M.; Komorovsky, S.; Ruud, K.; Kaupp, M. *J. Phys. Chem. A* **2015**, *119*, 12892.
(89) Sinnecker, S.; Neese, F.; Noodleman, L.; Lubitz, W. *J. Am. Chem. Soc.* **2004**, *126*, 2613.
(90) Perdew, J. P.; Burke, K.; Ernzerhof, M. *Phys. Rev. Lett.* **1996**, *77*, 3865.
(91) Pederson, M. R.; Khanna, S. N. *Phys. Rev. B: Condens. Matter Mater. Phys.* **1999**, *60*, 9566.
(92) Schmitt, S.; Jost, P.; Van Wüllen, C. *J. Chem. Phys.* **2011**, *134*, 194113.
(93) Neese, F. *J. Chem. Phys.* **2005**, *122*, 034107.
(94) Frisch, M. J.; Trucks, G. W.; Schlegel, H. B.; Scuseria, G. E.; Robb, M. A.; Cheeseman, J. R.; Scalmani, G.; Barone, V.; Mennucci, B.; Petersson, G. A.; Nakatsuji, H.; Caricato, M.; Li, X.; Hratchian, H. P.; Izmaylov, A. F.; Bloino, J.; Zheng, G.; Sonnenberg, J. L.; Hada, M.; Ehara, M.; Toyota, K.; Fukuda, R.; Hasegawa, J.; Ishida, M.; Nakajima, T.; Honda, Y.; Kitao, O.; Nakai, H.; Vreven, T.; Montgomery, J. A., Jr.; Peralta, J. E.; Ogliaro, F.; Bearpark, M. J.; Heyd, J.; Brothers, E. N.; Kudin, K. N.; Staroverov, V. N.; Kobayashi, R.; Normand, J.; Raghavachari, K.; Rendell, A. P.; Burant, J. C.; Iyengar, S. S.; Tomasi, J.; Cossi, M.; Rega, N.; Millam, N. J.; Klene, M.; Knox, J. E.; Cross, J. B.; Bakken, V.; Adamo, C.; Jaramillo, J.; Gomperts, R.; Stratmann, R. E.; Yazyev, O.; Austin, A. J.; Cammi, R.; Pomelli, C.; Ochterski, J. W.; Martin, R. L.; Morokuma, K.; Zakrzewski, V. G.; Voth, G. A.; Salvador, P.; Dannenberg, J. J.; Dapprich, S.; Daniels, A. D.; Farkas, Ö.; Foresman, J. B.; Ortiz, J. V.; Cioslowski, J.; Fox, D. J. *Gaussian 09*; Gaussian, Inc.: Wallingford, CT, 2009.

DOI: 10.1021/jacs.7b10148
J. Am. Chem. Soc. 2018, 140, 2135−2144